Progress In Electromagnetics Research, Vol. 138, 65–82, 2013

PLANAR MAGNETIC INDUCTION TOMOGRAPHY FOR 3D NEAR SUBSURFACE IMAGING

Lu Ma, Hsin-Yu Wei, and Manuchehr Soleimani*

Engineering Tomography Laboratory (ETL), Department of Electronic and Electrical Engineering, University of Bath, Bath, UK

Abstract—Magnetic induction tomography (MIT) is a tomographic technique utilising inductive coils and eddy currents to map the passive electromagnetic properties of an object. Eddy current methods are widely used for non-destructive testing (NDT) in inspection of metallic structures. Eddy current based NDT uses a single coil or a pair of coils to scan the samples. As an emerging NDT technique, MIT scans the sample with a coil array through an eddy current based tomographic approach. In this paper, a planar array MIT system (PMIT) is proposed for 3D near subsurface imaging. This is of great importance as there are large numbers of potential applications for MIT that allow limited access to the materials under testing. The system development, practical implication, capability and limitations of PMIT are discussed. The fundamental principles are demonstrated through simulations. Experimental data are used to evaluate the capability and detectability this system has as a potential 3D subsurface imaging tool.

1. INTRODUCTION

Magnetic Induction Tomography (MIT) is an emerging non-destructive evaluation technique that is able to map passive electromagnetic properties without causing material damage. In recent years, MIT has had applications ranging from biomedical imaging to industrial inspection. Many previous MIT systems were developed using coils that are arranged around the imaging periphery [1–7]. This type of coil arrangement has a circular geometry and free access around the complete periphery, thus full access tomography can be achieved. However, there are numerous applications where access is restricted and non-invasive measurements can only be taken from one surface [8].

Received 7 November 2012, Accepted 4 March 2013, Scheduled 15 March 2013

* Corresponding author: Manuchehr Soleimani (m.soleimani@bath.ac.uk).

Consequently, the imaging process cannot be carried out by using a MIT system with a circular or near circular sensor array. Planar geometry can overcome this difficulty. As such, recent research has focused on developing planar sensors and estimating near-surface material properties using them [9, 10]. Inspecting product quality using planar sensors is also possible [11]. A simulation study of planar MIT was reported in [8], where the 2D cross-sectional images of conductive bars were obtained using an iterative SIRT reconstruction. Paper [12] presented a planar MIT system for the detection of conductivity inhomogeneity on the surface of a metallic plate. The sensors were placed in a circular shape with their axes perpendicular to the plate. The 2D images were reconstructed using experimental data. It was shown that a spatial distinguish ability of 10–20% of the array diameter was possible. In this paper, a planar MIT (PMIT) is developed as a type of limited access tomography, which realises 3D reconstruction for near subsurface imaging. Recently, we have developed a 3D MIT system [13], and the techniques developed in 3D MIT enabled the development of a 3D PMIT, which offers an insight into the structures underneath the sensors by depth detection. The observations in this paper can be extended to other types of tomography and inverse problems [14–20]. The development of planar sensor model and system setup are presented, followed by simulation results and experimental evaluation. The paper presents the first 3D PMIT study for subsurface imaging. The PMIT has two main advantages over traditional scanning based eddy current NDT methods. Firstly, PMIT employs an array of coils so that the scanning speed can be improved. Secondly, measurements from non-neighboring coils offer greater depth detection compared to single coil or double coil based eddy current scanning techniques, which will help to gain information about the materials under testing.

Table 1. Sensor model parameters.

Parameters	Value
Number of coils	16
Number of turns for each coil	100
Inner diameter for each coil: d_i (cm)	3.9
Outer diameter for each coil: d_o (cm)	4.1
Coil height: H (cm)	5
Coil side length: l (cm)	3.4
Self-inductance of each coil (μH)	380

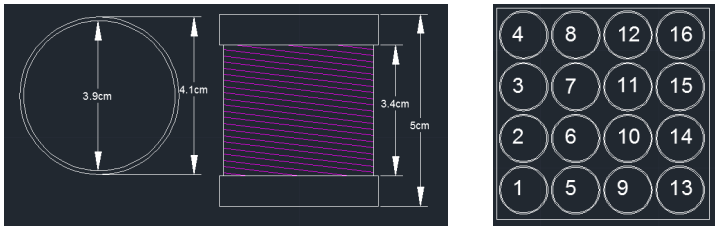

Figure 1. (a) Coil dimensions, (b) coil sequence.

2. SYSTEM DESCRIPTION

2.1. Sensor Model

The planar sensor array consists of 16 air-core cylindrical coils. The 16 coils are arranged in a 4×4 matrix form, and mounted on a non-conductive square board with a surface area of $18 \times 18\,\text{cm}^2$. The thickness of the board is $t = 0.3\,\text{cm}$. The distance between each coil is 0.3 cm. The important parameters for this sensor model are listed in Table 1. Figure 1(a) shows the coil dimensions, and Figure 1(b) shows the arrangement of coil sequence.

2.2. System Setup

This PMIT system consists of (i) a Topward 8112 digital function generator, (ii) a matrix of 16 equally spaced inductive coils, with each coil axis perpendicular to the materials under testing, (iii) an ADG406 16-channel multiplexer, (iv) a National Instrument (NI-6295) data acquisition card, and (v) a host computer. The block diagram of this system is given in Figure 2. Each of the 16 inductive coils is individually supplied with a 15 V peak, 50 kHz sinusoidal-signal from the digital function generator, while the remaining coils are floated as receivers. An ADG406 16-channel multiplexer is connected in the system to accomplish the channel switching process. A NI USB-6295 data acquisition device is connected through USB ports to interface between the ADG406 multiplexer and a host PC, where the image reconstruction takes place. The NI USB-6295 has four analog outputs at 16 bits and an input of max rate of 1.25 MS/s. The aim of this device is to collect individual data efficiently, combine data effectively and display data in images to suit the need for imaging process. This PMIT system has 120 unique coil pairs: 1-2, 1-3, ..., 1-16, 2-3, 2-4, ..., 15-16, giving a total number of 120 independent measurements.

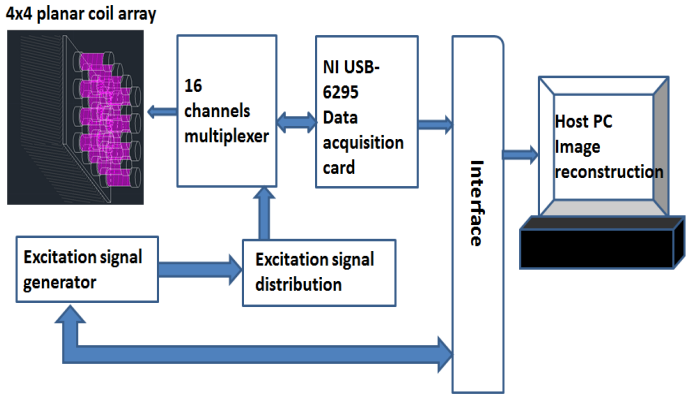

Figure 2. Block diagram of the proposed PMIT system.

All the measurements are averaged three times before being displayed to ensure low noise perturbation. The image reconstruction module extracts 120 independent measurements, performs the reconstruction algorithms, displays and updates the images.

The signal to noise ratio (SNR) is taken to indicate the signal level of this system to the background noise level, which can be defined using amplitude ratio as [21].

$$\mathrm{SNR} = 20 \log_{10} \frac{U_S}{U_N} \tag{1}$$

where U_S is the mean signal amplitude and U_N is the standard deviation of measured signal amplitude. It can be seen from Figure 3 that the highest SNR of this PMIT system is 63.1 dB (for measurement between coil 1 and coil 2) and the lowest SNR is 33.4 dB (for measurements between coil 1 and coil 16). The coil arrangement can be seen in Figure 1(b).

3. METHOD

The forward problem in PMIT is a well-known eddy current problem [22–25]. In this study, the eddy current problem is solved using a magnetic potential vector A.

$$\nabla \times \frac{1}{\mu} \nabla \times A + j\sigma\omega A = J_s \tag{2}$$

where μ is the magnetic permeability, σ the electrical conductivity, ω the angular frequency of the excitation current, and J_s the excitation

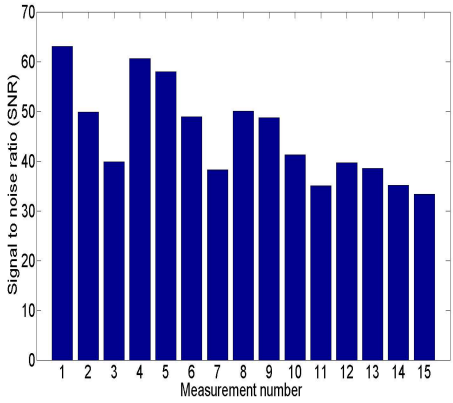

Figure 3. Signal to noise ratio of first cycle measurements when first coil used as excitation.

current density. The results from the forward problem will be used to calculate the induced voltages in sensing coils [26], as well as the Jacobian matrix which is needed for the inverse problem. An efficient formulation for the sensitivity map is used. If the total current in the excitation coil is I_0, the sensitivity of the induced voltage to the conductivity change can be written as [22, 25]:

$$\frac{\partial V_{mn}}{\partial \sigma_k} = -\omega^2 \frac{\int_{\Omega_k} A_m \cdot A_n dv}{I_0} \tag{3}$$

where V_{mn} is the measured voltage, σ_k the conductivity of voxel k, Ω_k the volume of the perturbation (voxel k), and A_m and A_n are respectively solutions of the forward solver when the excitation coil (m) is excited by I_0 and the sensing coil (n) excited with unit current. The sensitivity matrix J is constructed by subdividing the imaging region into small voxels and determining the change in measured voltage of each pair of sensors ΔV due to perturbations of the volume in each voxel.

In the previous section, the SNR is shown to indicate the signal level of the PMIT system. In this part, the sensitivity map will be used to evaluate how a pair of coils couple with each other. The sensitivity map of the electromagnetic imaging problem describes the system response to every voxel perturbation for a selected excitation/detection coil pair [5, 8, 22]. When the coils are close together, the system is sensitive to the surface layers, and as the coils become further apart, the sensitivity penetrates deeper underneath the object under testing [8]. This can be demonstrated by Figure 4, where a selection

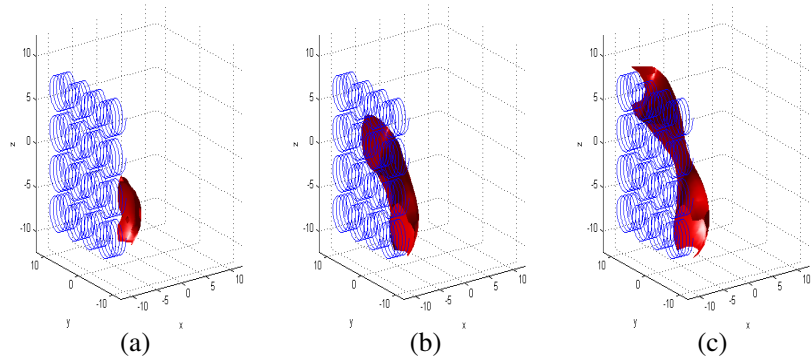

Figure 4. Sensitivity map coupling between: (a) coil 1 and coil 2, (b) coil 1 and coil 11 and (c) coil 1 and coil 16, the coil number sequence can be seen in Figure 1(b).

of sensitivity maps of this system are shown. When receiving coils are at an increased distanced from excitation coils, a relatively larger sensitive region and a greater penetration can be observed in the system response. A decreased sensitive contour can also be observed due to the decreased strength of signals from the receiving coils. This can be seen in Figure 4(c), showing a pair of coils with the greatest distance between them. The sensitive contour in Figure 4(c) has the deepest penetration and the largest area, but the sensitivity in the middle is lower compared to other patterns, as shown in Figures 4(a) and 4(b).

In this study, a linear inverse solver is used for 3D near subsurface imaging. In linear inversion, the forward problem is assumed to have a linear form: $\Delta V = J\Delta\sigma$. The Tikhonov regularization method has been commonly implemented for the MIT image reconstruction [4, 26, 27], particularly in [4]. Experimental validation of the Tikhonov method was shown using linear image reconstruction and in [26], where a nonlinear image reconstruction was demonstrated using both Tikhonov and total variation regularization methods. In this study, a standard Tikhonov regularization method is used as an inverse solver to calculate the conductivity distribution in the following manner:

$$\Delta\sigma = \left(J^T J + \alpha R\right)^{-1} J^T(\Delta V) \tag{4}$$

where ΔV is a column vector consisting of 120×1 changes of induced voltages, $\Delta\sigma$ also a column vector representing conductivity changes in $19^3 \times 1$ voxels, J a 120×19^3 matrix of the sensitivity field calculated from Equation (3), α the regularization parameter which is chosen empirically, and R an identity matrix.

4. SIMULATION AND EXPERIMENTAL EVALUATION

4.1. Detectability of PMIT System

The PMIT is a challenging 3D inverse problem, in particular, because of limited access to the object. The simulations presented in this section are used to study the underlying inverse problems in the context of a linear model. The end view of a number of simulation models are presented in Figure 5 to evaluate the capability and detectability of the PMIT system. The planar sensor array is simulated in (x, z) plane at $y = 0$. The first column in Figure 5 shows the simulated inclusions in different locations. The second column in Figure 5 includes the reconstructed images for each simulated case. The reconstructed 3D contour images in the third column in Figure 5 provide an insight as to where the inclusion is with respect to the planar sensor array.

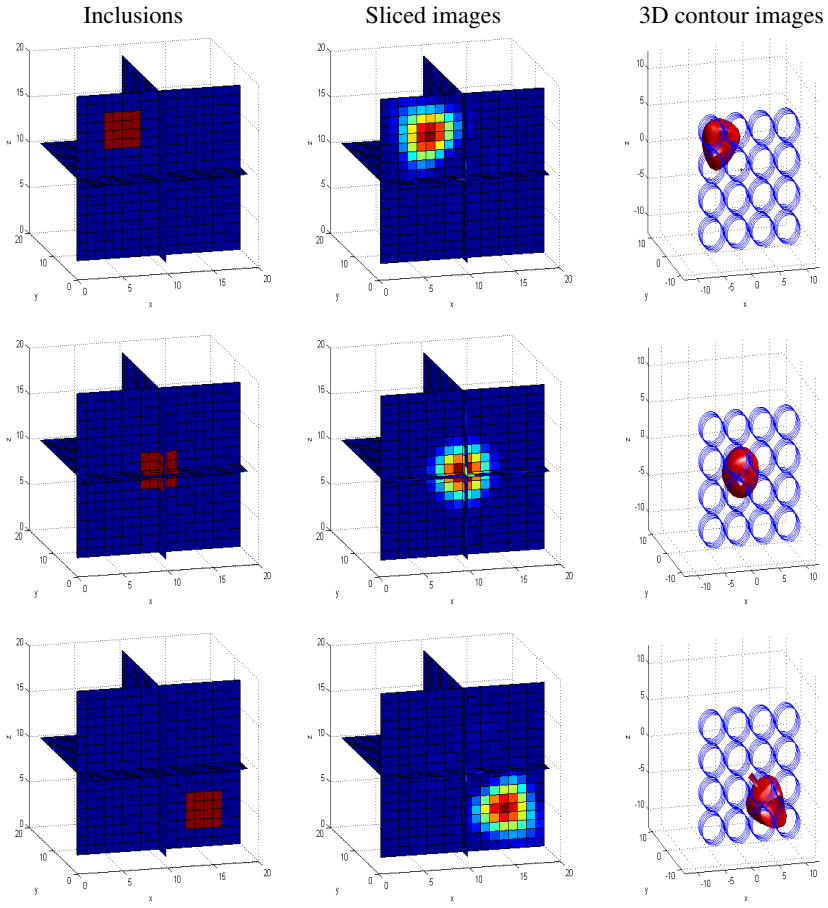

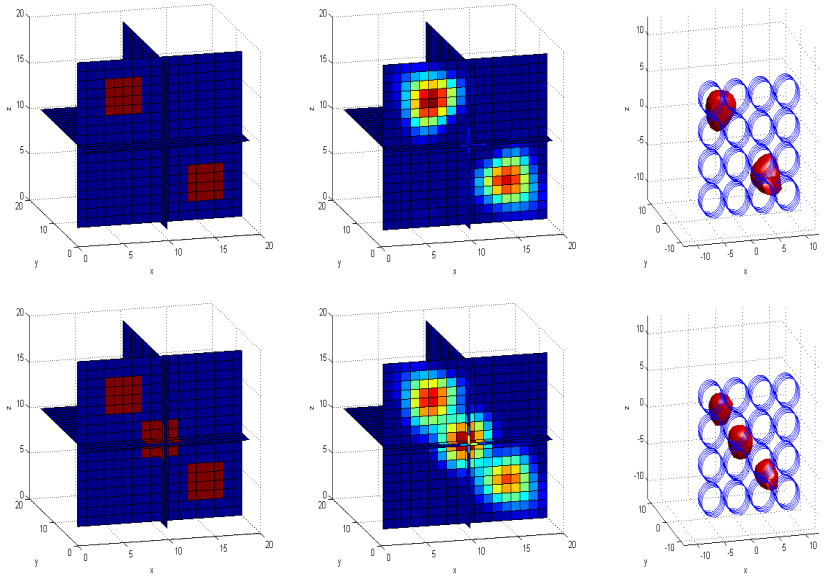

Figure 5. Detectability of PMIT using simulated data.

Aluminium rods of diameter 40 mm are used as test samples in our experiments to validate the simulations. These rods have a high electrical conductivity of 3.5×10^7 S/m and a relative permeability of 1. The first column in Figure 6 shows the positions of true aluminium rods in relation to the planar sensor array. The second column in Figure 6 shows the reconstructed images for each selected position. The reconstructed 3D contour images are included in the third column in Figure 6, where the end view of the rod positions with respect to the planar sensor model are shown. In these experiments, the aluminium rods are located against the planar sensor array with a fixed distance to the sensors. This fixed distance can be written as: $D_f = (H - l)/2 + t = 1.1$ cm, where H and l are the height and the side length of each coil sensor, and t is the thickness of the board.

4.2. Detectable Depth of PMIT System

In the previous section, we investigated the detectability of the PMIT system in terms of different positions using simulations and experiments. It was shown that this PMIT system is capable of detecting objects that are close to the sensors. For subsurface imaging, the imaging depth is a key parameter to assess the capability and detectability of this PMIT system. Therefore, a series of simulations and subsequent experiments are completed for this purpose.

In Figure 7, the top view of the simulation models are shown to demonstrate the principle of near subsurface imaging using PMIT system. The planar sensor model is simulated in (x, z) plane at $y = 0$.

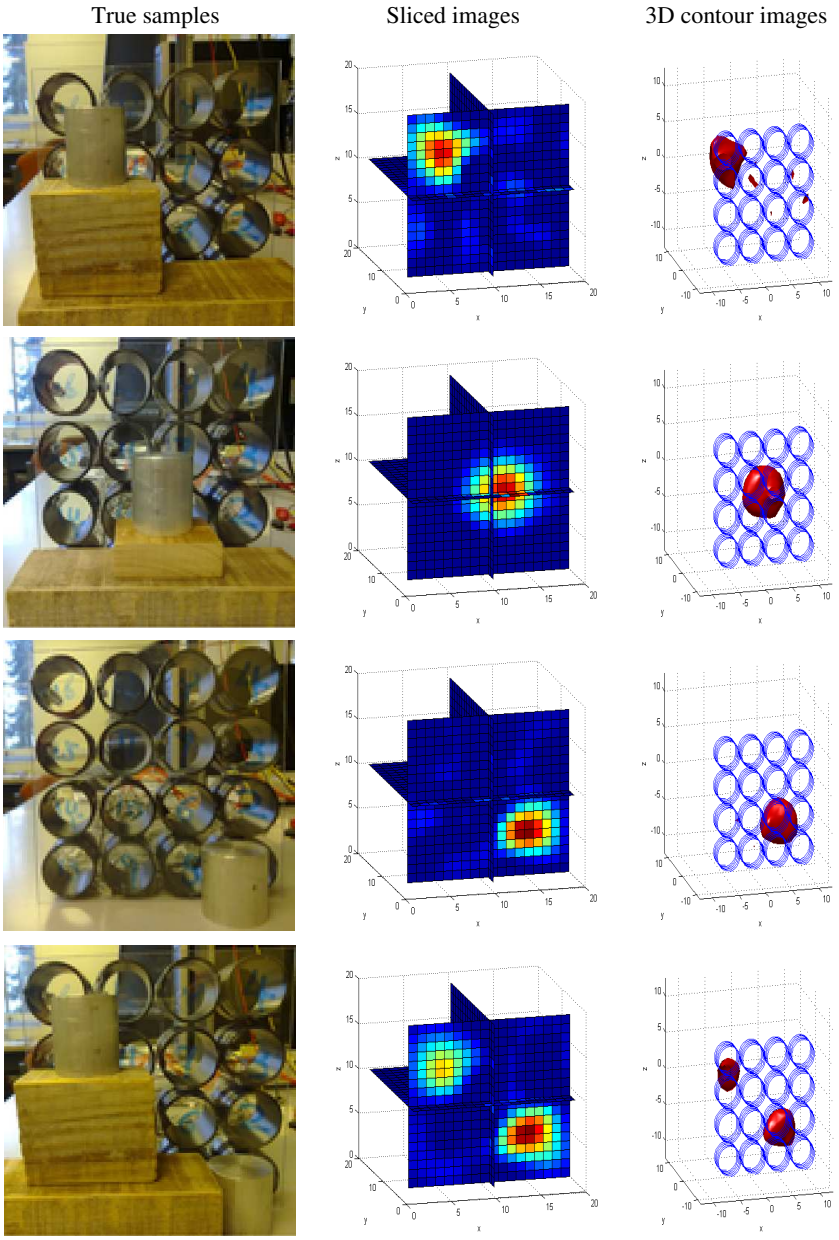

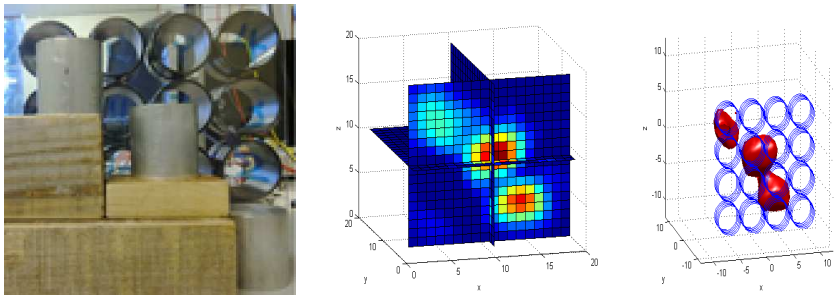

Figure 6. Detectability of PMIT using experimental data.

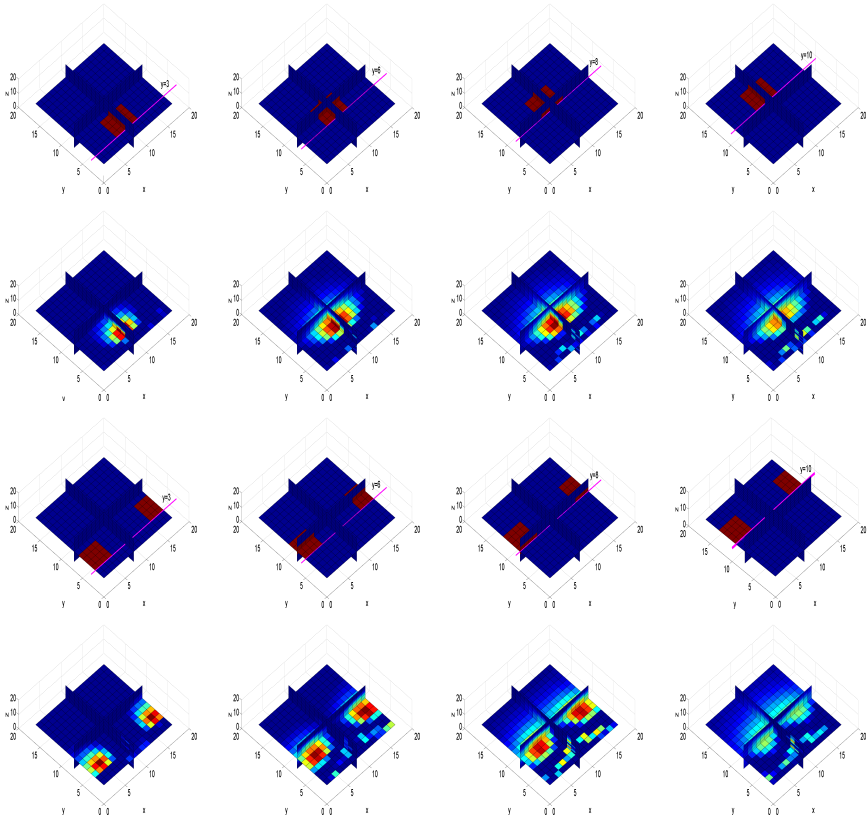

Figure 7. Depth detection using simulated data.

The first row in Figure 7 shows one simulated inclusion with highlighted lines indicating the distance between the sensors and the inclusion at four selected depths: $y = 3$, $y = 5$, $y = 8$, and $y = 10$. The second row

in Figure 7 presents the reconstruction of one inclusion at each selected depth. The same simulation procedures are adopted for simulating two inclusions, as shown in the third row in Figure 7. The reconstructed images are demonstrated in the bottom row in Figure 7. It can be seen from Figure 7 that the image quality degrades as the depth increases.

We have solved the inverse problem and detect a maximum imaging depth of 8–10 cm using simulations. In order to verify the simulation models and evaluate the detectable depth of the PMIT system using measured data, two sets of experiments are completed. Same aluminium rods are used as test samples. Figure 8 presents the experimental setup and the reconstructed images using one rod for subsurface imaging. The first row in Figure 8 shows the top view of the true samples with respect to the planar sensors.

As mentioned in Section 4.1, there is a fixed distance of $D_f = 1.1$ cm between the sensor array and the samples due to the construction of the sensor model and the thickness of the board. Although short, it is crucial to take this distance into consideration when evaluating the depth of this system, as it poses an additional barrier for eddy current in MIT, particularly as the skin depth is very limited under a low driving frequency of 50 kHz. Therefore, it cannot be neglected. The structure and layout of the sensor model need to be considered carefully if a highly accurate system is required. The moving distances from the planar sensors D_m are: 0 cm, 1 cm, 2 cm, 3 cm and 4 cm respectively. Therefore, the total distance between the true sample and the front of the sensor array is $D = D_f + D_m$. The

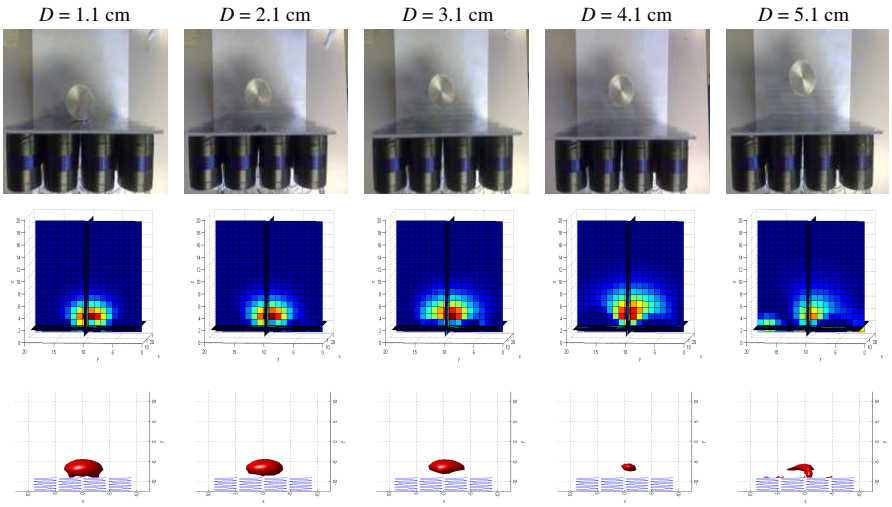

Figure 8. Depth detection using one object.

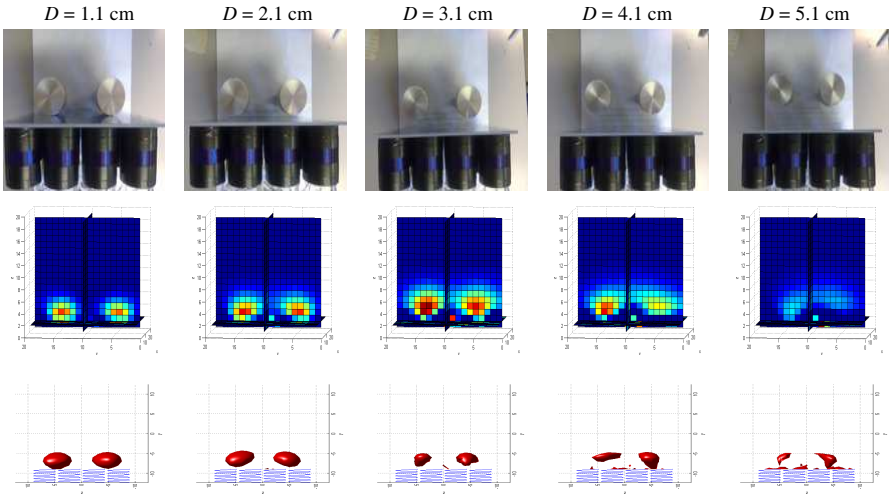

Figure 9. Depth detection using two objects.

sliced images and 3D contour images for each depth are presented in the second and third row in Figure 8.

The same experimental procedures are repeated using two rods, as shown in Figure 9. The distance between two aluminium rods is 4 cm. The true samples, sliced images and 3D contour images are shown in the first, second and third rows of Figure 9 respectively.

4.3. Quantitative Evaluation of Depth Detection for PMIT

Both simulations and experiments produce satisfactory reconstructions for object(s) close to the sensor array. In this section, we introduce an image quality parameter: volume deformation ratio (VDR) to examine the image quality degradation using experimental data for object(s) distanced from the sensor array.

It can be seen from Figures 8 and 9 that image reconstruction algorithms usually reconstruct a circular image to match the true object, and display it in a position that matches the true position of the target. As the object is distanced from the planar sensors, the system becomes less sensitive, and the measurements become less accurate. In this case, image algorithms will create a larger spherical image to represent the true target, resulting in artefacts around the boundary of the reconstructed image [28]. Therefore, the volume changes in reconstructed images due to the distance between sensors and objects under testing can be used to assess the image quality.

In order to calculate the VDR, a reference volume and a threshold

are required. Both simulations and experiments have shown that this PMIT system can detect object(s) close to the sensors, and can reconstruct satisfactory images. Therefore, we take the reconstructed image at this state (i.e., $D_m = 0\,\text{cm}$) as a reference image, and calculate the total volume of the inclusion(s) in the reconstructed image as a reference volume. The volume change Δv in the reconstructed image is proportional to the distance change Δd between the test sample(s) and the planar sensors within certain range. Finally, the slope $\frac{\Delta v}{\Delta d}$ can be used to represent the deformation rate. Let the threshold of VDR be 50%. If VDR is greater than 50%, we consider the reconstructed image to be too distorted to be of use.

The definition of VDR can be written in the following manner:

$$\text{VDR} = \left\| \frac{v_i - v_{ref}}{v_{ref}} \right\| \tag{5}$$

where v_i is the volume of the inclusion(s) in the reconstructed image with the object(s) placed at $i\,\text{cm}$ away from the planar array. The v_{ref} is the reference volume, which is taken from the volume of the reconstructed inclusion(s) with the object(s) placed are very close to the sensors (i.e., $D_m = 0\,\text{cm}$).

The volume of the inclusion(s) in reconstructed image can be calculated using the following equation [28]:

$$v = \frac{\sum \left[\Delta\sigma_k \geq \frac{1}{4}\max(\Delta\sigma)\right]}{\sum_1^i \Delta\sigma_i} \tag{6}$$

where $\Delta\sigma_k$ represents a voxel which has an amplitude greater than one-fourth of the maximum amplitude in the reconstructed image. Note that in the numerator, a threshold of one-fourth is chosen, which is the total number of voxels that contribute to most of the significant visual effects in the reconstructed image [28]. The denominator is the total number of voxels in reconstructed image. As each voxel has the same volume, the total volume of voxels can be calculated using the total number of the voxels.

It can be seen that from Equation (5) that if a reconstructed image is severely ill-posed, the VDR can be inaccurate as the total volume of the voxels might be extremely large ($v_i = +\infty$) or small ($v_i = -\infty$), or just happen to be the same as the reference volume ($v_i = v_{ref}$). In these cases, the VDR is not representative any more and cannot be taken into consideration for image quality assessment.

A threshold of 50% is chosen as the purpose of the experiments is to find the object(s) under testing rather than to examine the accuracy of the depth detection of our PMIT system. The threshold can be set lower if a higher sensitivity and accuracy are required.

4.4. Discussion

It can be seen from Figures 5 and 6 that the PMIT system is capable of detecting both single and multiple conductive objects, which are placed with an approximate fixed distance of 1 cm away from the sensors. However, the reconstructed images using experimental data showing in Figure 6 are generally compromised compared to the results presented in Figure 5.

A number of simulation models in Figure 7 demonstrate the principles of near subsurface imaging using a PMIT system. It can be seen from Figure 7 that a depth of 8–10 cm can be achieved through simulations. This further validates our system sensitivity analysis, as presented in Figure 4, where the sensitive contour does not penetrate more than 10 cm into the imaging region. The experimental results presented in Figures 8 and 9 reveal that the PMIT system can detect a depth of approximately 3–4 cm beneath the planar array.

It is clear from the 3D contour images shown in Figure 8 that the true sample can only be detected partially as the distance from the sensors increases. Moreover, comparing the reconstructed images from two sets of experiments for evaluating depth detection, a rapid degradation in image quality can be observed in Figure 9 compared to the results in Figure 8. This image degradation is also quantitatively

Table 2. Volume deformation ratio.

Moving distance	1 cm	2 cm	3 cm	4 cm
VDR one object	1.54%	15.74%	41.48%	53.60%
VDR two objects	12.01%	42.55%	51.45%	56.13%

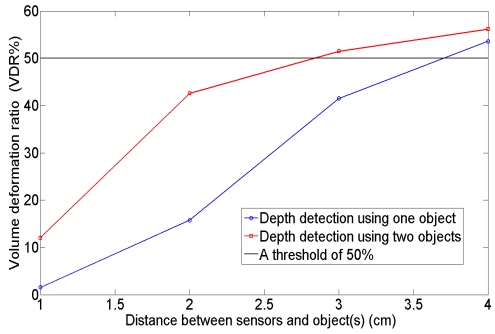

Figure 10. Graph of volume deformation.

evaluated through an image quality measure VDR, as shown in Table 2 and Figure 10. The VDR of the reconstructed image at incrementally increased distance of 1 cm for one object is 1.54%, while the VDR for two objects at the same distance away from planar sensors is 12.01%, significantly higher. As the distance is increased to 3 cm, the VDR for two objects exceeds the threshold of VDR, which means the reconstructed image is severely degraded. However, this degradation in image quality is not associated with the number of objects under testing. The system detectability depends on the distribution of the sensitive region and the locations of the object(s) under testing.

In general, uniform detectability can be observed in the region that is close to the sensors. As the imaging depth increases, the sensitivity degrades from uniform detectability. The detectable area can be considered similar to a spherical region due to the decreased signals between coil pairs that are further away. It is shown in Figure 4(c) that the measurement from the furthest coil pair contribute to most of the significant depth. However, the furthest coil pairs also have the lowest SNR, as shown in Figure 3, which means the sensitivity of such a coil pair is reduced compared to the sensitivity of neighbouring coil pairs. As the object moves further away from the planar sensors, the overall sensitivity decreases. The areas that are close to the edge of the planar array is comparatively less covered by the sensor array. Hence, the sensitive region tends to have a trapezoidal or spherical shape, as shown in Figure 11.

The level of detectability between simulated and measured data differs for two reasons: noise in measured data, and the skin depth effect. In this study, at a driving frequency of 50 kHz, aluminium has a skin depth of approximately 366 μm [4], which is far less than the diameter of the aluminium rod. This results in the eddy current threading on the surface of the object. As such, very little information can be obtained from the back of the test sample. The simulated models do not have issues associated with depth penetration as a linear model is assumed.

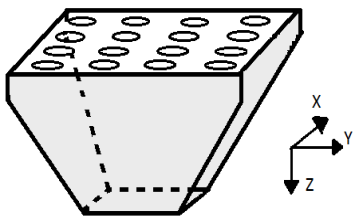

Figure 11. The distribution of sensitive region against the imaging depth.

5. CONCLUSIONS

This paper investigates the capability and detectability of a novel PMIT system. This geometry makes it possible to study the near subsurface imaging using an eddy current method. It is a very challenging imaging setup as access to the targeted object is limited to one surface only. The fundamental principles are verified through simulation studies. Experimental results detect a limited depth in this PMIT system. Nevertheless, it demonstrates the potential this system has as a non-invasive subsurface imaging tool. In our future work, we will aim to improve the depth detection by developing a multi-frequency PMIT system. Non-linear image reconstruction in 3D PMIT will also be a subject of our future study.

REFERENCES

1. Wei, H.-Y. and M. Soleimani, "Two-phase low conductivity flow imaging using magnetic induction tomography," *Progress In Electromagnetics Research*, Vol. 131, 97–115, 2012.
2. Ma, L., H.-Y. Wei, and M. Soleimani, "Pipeline inspection using magnetic induction tomography based on a narrowband pass filtering method," *Progress In Electromagnetics Research M*, Vol. 23, 65–78, 2012.
3. Lyon, G. M., Z. Z. Yu, A. J. Peyton, and M. S. Beck, "Developments in electro-magnetic tomography instrumentation," *IEEE Colloguium on Advances in Electrical Tomography*, Vol. 12, 1–4, 1993.
4. Ma, X., A. J. Peyton, S. R. Higson, A. Lyons, and S. J. Dickinson, "Hardware and software design for an electromagnetic induction tomography (EMT) system for high contrast metal process applications," *Measurement Science and Technology*, Vol. 17, No. 1, 111–118, 2006.
5. Peyton, A. J., Z. Z. Yu, G. Lyon, S. Al-Zeibak, J. Ferreira, J. Velez, F. Linhares, A. R. Borges, H. L. Xiong, N. H. Saunders, and M. S. Beck, "An overview of electromagnetic induction tomography: Description of three different systems," *Measurement Science and Technology*, Vol. 7, 261–271, 1996.
6. Yu, Z. Z., A. J. Peyton, W. F. Conway, L. A. Xu, and M. S. Beck, "Imaging system based on electromagnetic tomography (EMT)," *Electronics Letters*, Vol. 29, No. 7, 625–626, 1993.
7. Korjenevsky, A., V. Cherepenin, and S. Sapetsky, "Magnetic

induction tomography: Experimental realization," *Physiological Measurement*, Vol. 21, No. 1, 89, 2000.

8. Ramli, S. and A. J. Peyton, "Feasibility study of planar-array electromagnetic inductance tomography (EMT)," *1st World Congress on Industrial Process Tomography*, Buxton, Greater Manchester, Apr. 14–17, 1999.
9. Mukhopadhyay, S. C., S. Yamada, and M. Iwahara, "Inspection of electro-plated materials-performance comparison with planar meander and mesh type magnetic sensor," *International Journal of Applied Electromagnetics and Mechanics*, Vol. 15, No. 1, 323–330, 2002.
10. Mukhopadhyay, S. C., S. Yamada, and M. Iwahara, "Investigation of near-surface material properties using planar type meander coil," *JSAEM Studies on Applied Electromagnetics and Mechanics*, Vol. 11, 61–69, 2001.
11. Mukhopadhyay, S. C., "Novel planar electromagnetic sensors: Modeling and performance evaluation," *Sensors*, Vol. 5, No. 12, 546–579, 2005.
12. Yin, W. and A. J. Peyton, "A planar EMT system for the detection of faults on thin metallic plates," *Physiological Measurement*, Vol. 17, No. 8, 2130–2135, 2006.
13. Wei, H. Y., L. Ma, and M. Soleimani, "Volumetric magnetic induction tomography," *Measurement Science and Technology*, Vol. 23, No. 5, 055401, 2012.
14. Hajihashemi, M. R. and M. El-Shenawee, "Inverse scattering of three-dimensional PEC objects using the level-set method," *Progress In Electromagnetics Research*, Vol. 116, 23–47, 2011.
15. Park, W.-K., "On the imaging of thin dielectric inclusions via topological derivative concept," *Progress In Electromagnetics Research*, Vol. 110, 237–252, 2010.
16. Banasiak, R., Z. Ye, and M. Soleimani, "Improving three-dimensional electrical capacitance tomography imaging using approximation error model theory," *Journal of Electromagnetic Waves and Applications*, Vol. 23, Nos. 2–3, 411–421, 2012.
17. AlShehri, S. A., S. Khatun, A. B. Jantan, R. S. A. Raja Abdullah, R. Mahmood, and Z. Awang, "3D experimental detection and discrimination of malignant and benign breast tumor using NN-based UWB imaging system," *Progress In Electromagnetics Research*, Vol. 116, 221–237, 2011.
18. Ren, S., W. Chang, T. Jin, and Z. Wang, "Automated SAR reference image preparation for navigation," *Progress In*

Electromagnetics Research, Vol. 121, 535–555, 2011.

19. Wei, S.-J., X.-L. Zhang, J. Shi, and G. Xiang, "Sparse reconstruction for SAR imaging based on compressed sensing," *Progress In Electromagnetics Research*, Vol. 109, 63–81, 2010.
20. Chang, Y.-L., C.-Y. Chiang, and K.-S. Chen, "SAR image simulation with application to target recognition," *Progress In Electromagnetics Research*, Vol. 119, 35–57, 2011.
21. Merwa, R. and H. Scharfetter, "Magnetic-induction-tomography: Evaluation of the point-spread-function and analysis of resolution and image distortion," *Physiological Measurement*, Vol. 28, 313–324, 2007.
22. Dyck, D. N., D. A. Lowther, and E. M. Freeman, "A method of computing the sensitivity of the electromagnetic quantities to changes in the material and sources," *IEEE Transactions on Magnetics*, Vol. 30, 3415–3418, 1994.
23. Griffiths, H., "Magnetic induction tomography," *Measurement Science and Technology*, Vol. 12, 1126–1131, 2001.
24. Ktistis, C., D. W. Armitage, and A. J. Peyton, "Calculation of the forward problem for absolute image reconstruction in mit," *Physiological Measurement*, Vol. 29, S455–S464, 2008.
25. Soleimani, M. and W. R. B. Lionheart, "Image reconstruction in three-dimensional magnetostatic permeability tomography," *IEEE Transactions on Magnetics*, Vol. 41, 1274–1279, 2005.
26. Soleimani, M., W. R. B. Lionheart, A. J. Peyton, X. Ma, and S. R. Higson, "A three-dimensional inverse finite-element method applied to experimental eddy-current imaging data," *IEEE Transactions on Magnetics*, Vol. 42, No. 5, 1560–1567, 2006.
27. Ziolkowski, M., S. Gratkowski, and R. Palka, "Solution of three dimensional inverse problem of magnetic induction tomography using Tikhonov regularization method," *International Journal of Applied Electromagnetics and Mechanics*, Vol. 30, No. 3–4, 245–253, 2009.
28. Adler, A., J. H. Arnold, R. Bayford, A. Borsic, B. Brwon, P. Dixon, T. J. C. Faes, I. Frerichs, H. Gagnon, Y. Garbr, B. Grychtol, G. Hahn, W. R. B. Lionheart, A. Malik, R. P. Patterson, J. Stocks, A. Tizzard, N. Weiler, and G. K. Wolf, "Greit: A unified approach to 2D linear EIT reconstruction of lung images," *Physiological Measurement*, Vol. 30, S33–S55, 2009.